JGR Solid Earth

RESEARCH ARTICLE
10.1029/2021JB023157

Shallow Aseismic Slip in the Delaware Basin Determined by Sentinel-1 InSAR

K. S. Pepin[1], W. L. Ellsworth[1], Y. Sheng[1,2], and H. A. Zebker[1]

[1]Department of Geophysics, Stanford University, Stanford, CA, USA, [2]Institut des Sciences de la Terre, Université Grenoble Alpes, Grenoble, France

Key Points:

- Linear deformation features in the southeastern portion of the Delaware Basin are attributed to aseismic slip on normal faults
- Identified faults create graben structures that likely belong to a larger graben network
- Aseismic and seismic fault movement in Texas' Delaware Basin can be linked to wastewater injection in the Delaware Mountain group

Supporting Information:

Supporting Information may be found in the online version of this article.

Correspondence to:

K. S. Pepin,
kspepin@stanford.edu

Citation:

Pepin, K. S., Ellsworth, W. L., Sheng, Y., & Zebker, H. A. (2022). Shallow aseismic slip in the Delaware Basin determined by Sentinel-1 InSAR. *Journal of Geophysical Research: Solid Earth*, *127*, e2021JB023157. https://doi.org/10.1029/2021JB023157

Received 1 SEP 2021
Accepted 23 JAN 2022

Author Contributions:

Conceptualization: K. S. Pepin, W. L. Ellsworth, Y. Sheng, H. A. Zebker
Data curation: K. S. Pepin, Y. Sheng
Formal analysis: K. S. Pepin, W. L. Ellsworth
Funding acquisition: W. L. Ellsworth, H. A. Zebker
Investigation: K. S. Pepin
Methodology: K. S. Pepin, W. L. Ellsworth, H. A. Zebker
Resources: K. S. Pepin
Software: K. S. Pepin
Supervision: W. L. Ellsworth, H. A. Zebker
Validation: K. S. Pepin
Visualization: K. S. Pepin
Writing – original draft: K. S. Pepin
Writing – review & editing: K. S. Pepin, W. L. Ellsworth, Y. Sheng, H. A. Zebker

Abstract The Delaware Basin, Texas is currently a hot-spot of induced seismicity and ground deformation due to fluid extraction and injection associated with horizontal drilling techniques; however, the driving mechanism behind the seismicity and deformation remains under debate. Using vertical and east-west horizontal surface deformation measurements derived from Sentinel-1 interferometric synthetic aperture radar (InSAR), we show that the subsurface responds differently to oil and gas activity in the northern and southeastern portions of the basin. In the north, where there is little seismicity, deformation patterns display long-wavelengths and equidimensional patterns. In contrast, the southeast region hosts most of the seismicity and displays spatial deformation patterns with narrow linear features that strike parallel to the maximum principal horizontal stress and to trends in seismicity, suggesting movement along normal faults. We model a linear deformation feature using edge dislocations and show that the InSAR observations can be reproduced by slip on normal faults contained within the Delaware Mountain Group (DMG), the formation that hosts local wastewater injection and the majority of earthquakes. Our model consists of three parallel, high-angle normal faults, with two dipping toward one another in a graben structure. Slip magnitudes reach up to 25 cm and are spatially correlated with injection wells. Measured seismicity can only explain ~2% of the fault motion predicted by our fault model, suggesting that slip leading to the deformation is predominantly aseismic. We conclude that seismic and aseismic fault motion in the southeastern Delaware Basin is likely driven by wastewater injection near critically-stressed normal faults within the DMG.

Plain Language Summary In the Delaware Basin, TX, widespread oil and gas operations have been linked to an increase in earthquake frequency and ground deformation. We use satellites to measure the ground deformation and show that the northern and southern portions of the basin respond differently to the pumping and injection of fluids. The southern portion displays narrow linear displacement patterns, whereas the northern region displays wide and equidimensional features. The relationship of the narrow features in the southern portion of the basin to local stress conditions and earthquake locations suggests downward slip on faults. Using analytic models in a small study area, we develop a three-fault slip model that is consistent with ground displacement measurements, the location and sense of slip of the largest local earthquakes, and wastewater disposal wells. Our findings suggest that wastewater disposal in the Delaware Mountain group is reactivating pre-existing normal faults, leading to induced earthquakes and non-seismic slip.

1. Introduction

The Delaware Basin is a giant oil and gas field in the Permian Basin, covering an extensive portion (22,000 km^2) of West Texas and southeastern New Mexico (Figure 1a inset). After being heavily exploited in the 20th century via conventional vertical production, 2009 brought a resurgence in oil and gas activity due to the development of organic rich shale beds using horizontal drilling and hydraulic fracturing (a.k.a. "unconventional") techniques. Similar to what has been observed in oil fields around the world, the Delaware Basin experienced an uptick in seismic activity coincident with unconventional development, leading many seismologists to infer those earthquakes were being induced by the development itself (e.g., Frohlich et al., 2016; Skoumal et al., 2020). Consequently, the state of Texas funded deployment of a regional seismic network, the TexNet array (Savvaidis et al., 2019), to better detect the regional seismicity and determine the underlying causes. The network has recorded thousands of small-to-moderate earthquakes in the Delaware Basin since its deployment in January 2017, including a M_W 4.8 event on 26 March 2020 (Figure 1a). These events are mainly concentrated in the southeastern portion of the Delaware Basin in Reeves county, despite widespread oil and gas activity throughout the basin (Figure 1b).

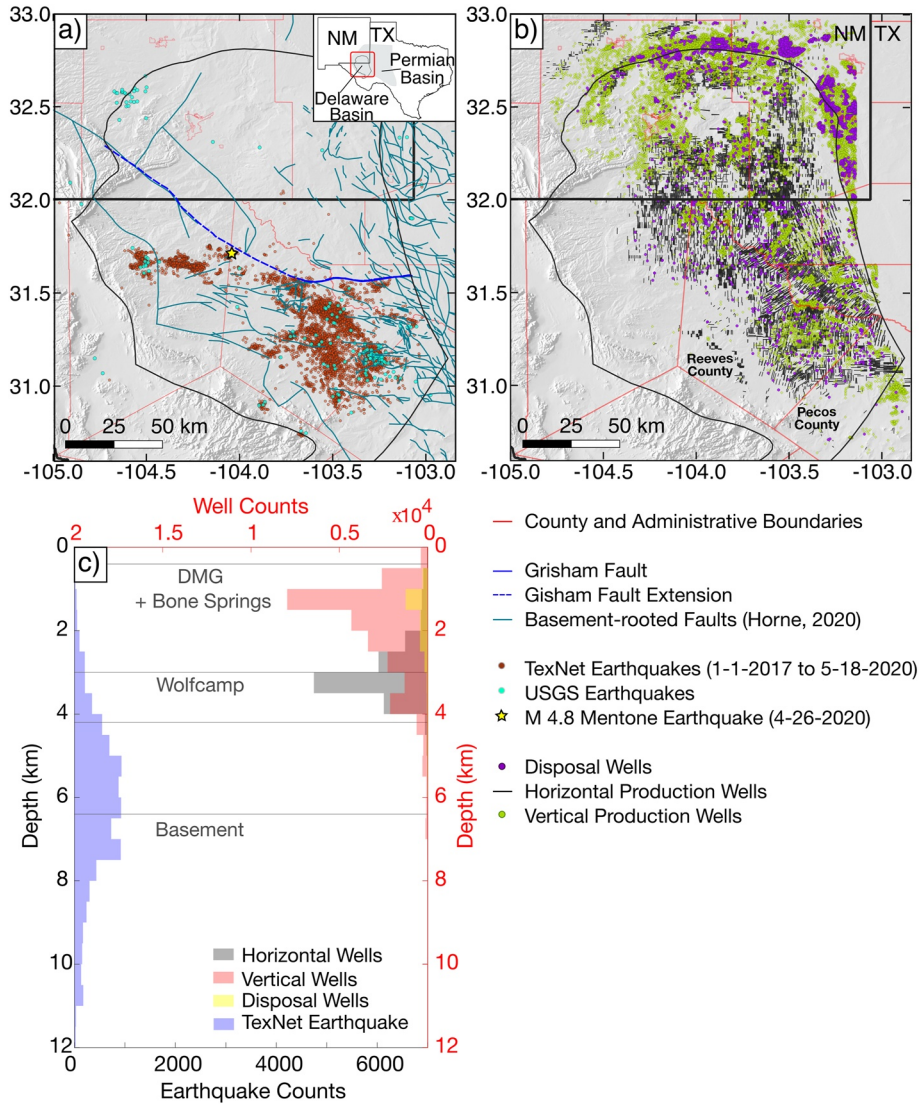

Figure 1. Seismicity, fault-mapping, and oil and gas activity in the Delaware Basin. (a) The seismic activity recorded by the USGS and TexNet arrays is concentrated in the southeastern Delaware Basin, below the Grisham Fault and its extension. Besides this distinction, few other faults show spatial correlations with seismic trends. (b) shows the disposal and productions wells that were active at some point between Dec 2014–June 2020 and assigned to the Delaware Basin (downloaded from Enverus, 1999). In contrast to the seismicity, oil and gas activity is widespread throughout the basin. (c) Earthquake depths from the TexNet catalog span a wide range, including into the basement, but these depths are highly uncertain. Most of the injection is concentrated above 3 km depth and above the producing shales. The formation depths depicted in (c) are approximate averages that we developed from formation surfaces provided by Enverus (1999); the true depth ranges vary throughout the basin. Fault traces provided by Horne, 2020.

The low density of earthquakes to the north of the Grisham fault (Figure 1a) is likely due to low pore pressure conditions caused by decades of conventional oil and gas activity prior to the 21st century; however, the geomechanical mechanisms leading to the onset of seismic activity to the south of the Grisham fault since 2009 remain under debate (Dvory & Zoback, 2021; Hennings et al., 2021). Within the seismically active portion of the basin, the dense concentration of old vertical, new horizontal, and disposal wells (Figure 1b) makes it challenging to determine the most probable industrial drivers, since hydraulic fracturing ("fracking"), fluid production, and wastewater injection can all lead to induced seismicity (see Ellsworth, 2013; Schultz et al., 2020; Suckale, 2010, respectively, for reviews on these topics). For instance, hydraulic fracking is considered a major cause of induced events in western Canada (e.g., Farahbod et al., 2015), whereas earthquakes near the Wilmington Field in California have been linked to extreme subsidence and stress changes from oil and gas production (Kovach, 1974).

The most-commonly cited mechanism, however, is wastewater injection, where fluid and increased pore pressure propagate to pre-existing faults, reducing normal stress and allowing seismic rupture (Ellsworth, 2013). Indeed, in nearby Oklahoma, where there have been a number of large-magnitude induced earthquakes ($M_W > 5$), studies strongly suggest that deep wastewater disposal near basement faults is the driving mechanism (Grandin et al., 2017; Keranen et al., 2013; Yeck et al., 2017).

In the Delaware Basin, the majority of wastewater disposal occurs in the Delaware Mountain Group (DMG), which lies above the producing shales (Wolfcamp) and 3–4 km above the basement in much of the producing portion of the basin (Figure 1c). In addition, there are few publicly-mapped faults in Reeves county and none of them extend from the DMG into the basement. Therefore, it is unlikely that basement faults are being induced to failure by wastewater disposal, as observed in nearby Oklahoma or elsewhere in Texas (Frohlich et al., 2014; 2016; Hornbach et al., 2015) unless poroelastic effects are the dominant mechanism (Zhai et al., 2021). An additional hurdle is the difficulty of linking specific events to any group of wells, due to the large depth uncertainty in earthquake hypocenters. Earthquakes in the southern Delaware Basin in the TexNet catalog range in depth between 0 and 19 km relative to ground surface (Figure 1c), with an average depth of 6 km and mean uncertainty of 1.9 km. Lomax and Savvaidis (2019) studied absolute depth errors in the basin and found a narrower depth range when a near station provided some depth control, but also large uncertainties of approximately 4–5 km. Because the average depth separation between disposal wells in the DMG and the production wells in the Wolfcamp is only 1.2 km, the formal uncertainty can move an earthquake from an injection formation to a producing one, or from a producing formation to the basement, and vice versa.

Despite these challenges, recent works attribute seismicity in the Delaware Basin to both hydraulic fracking and wastewater injection. Savvaidis et al. (2020) link clusters of events to fracking operations via temporal and spatial correlations and also highlight a causal link between wastewater disposal and seismicity in a few isolated cases where hydraulic fracking could be ruled out. However, in regions where fracking and disposal overlap, it remains challenging to distinguish between the two sources. On the other hand, Skoumal et al. (2020) attributed the majority of the seismicity to wastewater disposal, with just ~5% of the earthquakes induced by hydraulic fracturing operations. Another recent study uses poroelastic modeling to show that wastewater disposal at selected wells leads to pore pressure changes sufficient to induce earthquakes (Deng et al., 2020); however, they do not yet explain the absence of earthquakes near the majority of disposal wells in the basin, other than to posit that there are no favorably oriented pre-existing fault planes nearby. Zhai et al. (2021) also use poroelastic modeling to hypothesize that basement seismicity could be explained by poroelastic effects due to shallow injection within the DMG, though the evidence supporting earthquakes in the basement remains highly uncertain.

To better understand the geomechanical connections between industry operations and induced seismicity, it is essential to constrain earthquake depths, determine how the subsurface is responding to well activity, and locate faults hosting seismicity. In some instances, addressing one or both of the first two objectives may illuminate the geometry and behavior of unmapped faults. For example, precision earthquake locations and focal mechanisms, and measured surface deformation from co- and inter-seismic displacements can be combined to define faults and determine the sense and magnitude of slip (e.g., Massonnet & Feigl, 1995; Weston et al., 2012). These techniques are especially feasible when investigating shallow, large-magnitude earthquakes, of which there are currently none in the Delaware Basin. Most of the observed events only have $M_W < 4$, making co-seismic deformation analysis challenging, though not impossible (for instance, Staniewicz et al. (2021) have shown ~0.7 cm of co-seismic deformation related to the M_W 4.8 Mentone earthquake (Figure 1a). Nevertheless, using methods of interferometric synthetic aperture radar (InSAR), a remote sensing technique capable of measuring mm-scale surface displacements in low-noise regions at 5–20 m native spatial resolution (but often reduced to tens to a few hundred meters spatial resolution), we will show that deformation in the Delaware Basin defines fault geometries and sheds light on the difference between the northern (non-seismic) and southeastern (seismic) zones of the region.

The use of InSAR to study the Delaware Basin has been growing in recent years. Kim and Lu (2018) used Sentinel-1 InSAR to map spatially isolated deformation signals and attributed them to subsurface causes, including karst dissolution at the Wink Sink and oilfield activity (see also Kim et al., 2019). In particular, the authors identified local instances of production-induced subsidence and injection-induced uplift. Both Deng et al. (2020) and Zhai et al. (2021) measured one component of deformation (a single Sentinel-1 radar line-of-sight look direction) to analyze the poroelastic pressure changes due to pumping and disposal, and included groundwater extraction as a possible source of subsidence. They also provided a wider look at the general deformation features in Reeves

County. Staniewicz et al. (2020) further extended InSAR to the greater Permian Basin, using two overlapping Sentinel-1 passes (two look directions) over the Central Basin Platform and the eastern half of the Delaware Basin. They noted a significant component of east-west horizontal motion in Reeves and Pecos counties, where the highest density of induced earthquakes occurs. These studies highlight the existence of non-tectonic deformation in the basin and demonstrate that geodesy may be an invaluable tool for understanding the subsurface response to oil and gas operations in this region.

In this paper, we first use Sentinel-1 InSAR to develop a basin-scale look at the vertical and east-west horizontal displacements in the Delaware Basin. The measurements reveal multiple linear deformation zones in the southeastern portion of the basin where seismic activity is concentrated. These features could be a result of slip on normal faults, a possibility that was also explored by Staniewicz et al. (2020), though they restricted their modeling to the vertical component of displacement. After motivating the consideration of fault slip, we determine the geometry and slip of potential faults using analytic modeling of both vertical and east-west horizontal displacements, focusing on a small study area along the border of Reeves and Pecos counties (see Figure 1b). We compare our results to an improved seismic analysis in the same study area, which is presented in a companion paper by Sheng et al. (2022a). In that work, they used a moment tensor analysis to determine focal mechanisms and depths for nine moderate events ($M_W > 2.7$), and phase arrival times to determine the depths of smaller earthquakes. When considered together, our study and Sheng et al. (2022a) suggest high-angle normal faults in the Delaware Mountain Group are activated by wastewater injection. We conclude with a discussion of the implications for the nature of induced seismicity in the greater Delaware Basin.

2. Sentinel-1 InSAR

2.1. Methods: InSAR Processing for Cumulative Displacements

The InSAR processing method we use to study the Delaware Basin consists of four main parts. First, we create geocoded single-look-complex (SLC) images at fine resolution (approximately 3.75 × 15 m) in three orbit sets (ascending paths 151 and 78, and descending path 85; Figure S1 in Supporting Information S1), using software developed by the Stanford Radar Group (Zebker, 2017; Zheng & Zebker, 2017). We remove SLCs with high atmospheric noise, resulting in 100 (Path 151), 108 (Path 78), and 109 (Path 85) SLCs between December 2014–June 2020 (Figure S2 in Supporting Information S1). Next, we calculate all interferograms formed from SLCs spaced 400 days apart or less (resulting in 1791 (Path 151), 2448 (Path 78), and 2197 (Path 85) interferograms), and spatially-average to ∼225 m pixel spacing (60 × 15 looks). Then, we unwrap the interferograms using the Statistical-cost, Network-flow Algorithm for PHase Unwrapping (SNAPHU) (Chen & Zebker, 2001) and remove the dry atmospheric phase, as described in Pepin et al. (2020).

Many of the unwrapped interferograms showed strong and broad atmospheric signals reaching ±10 cm. To reduce the contribution of these signals, we applied a high-pass filter to each interferogram (Pepin et al., 2020; Text S1 in Supporting Information S1). To determine the cumulative displacement in each look direction, we used a regularized SBAS inversion (Berardino et al., 2002) to create three line-of-sight (LOS) time series. We selected a maximum temporal baseline of 400 days to reduce the remaining atmospheric contributions (via the inclusion of many interferograms), which are random in time. The results for each orbit are shown in Figure S3 in Supporting Information S1, which display strong agreement in displacement patterns between ascending and descending paths. The observed consistency suggests that our processing decisions resulted in robust estimates of surface displacements, despite being computationally expensive, and that the majority of displacement is vertical. Text S1 and Figures S4–S6 in Supporting Information S1 provide further information about the LOS InSAR processing and agreement between the ascending orbits (Figure S4 in Supporting Information S1) and to local GPS stations (Figures S5–S6 in Supporting Information S1).

In the last stage, we combine and decompose these three data sets into time series of vertical and east-west horizontal displacements. Because we will be jointly analyzing both components of cumulative deformation, this final step warrants a detailed explanation. First, we resample each LOS time series to a uniform set of dates between 4 March 2015–31 March 2020 with 18 days spacing (Figure S2 in Supporting Information S1) and reference each to zero displacement on 4 March 2015. We then combine these two data sets into a "composite" ascending time series by scaling Path 151 such that it approximately corresponds to the expected displacement as viewed by Path 78. Since the majority of the displacement appears to be vertical, we approximate the scaling factor at each pixel

based on the relative projection of the LOS vectors onto the vertical component, that is, the ratio of the cosines of the incidence angles (θ_i) (in this case, $\frac{\cos\ \theta_{i-78}}{\cos\ \theta_{i-151}} \approx 0.86$). We then calculate the arithmetic mean at pixels where the two orbits overlap. We adopt the LOS unit vectors for Path 78 as the composite ascending unit vectors in further analyses. Finally, we decompose the descending and composite ascending LOS time series into vertical (V) and east-west horizontal (H_{ew}) displacements via the following relationship, which assumes zero north-south motion:

$$\begin{bmatrix} d \\ a \end{bmatrix} = \begin{bmatrix} \mathrm{los}_{d-v} & \mathrm{los}_{d-ew} \\ \mathrm{los}_{a-v} & \mathrm{los}_{a-ew} \end{bmatrix} \begin{bmatrix} V \\ H_{ew} \end{bmatrix}, \quad (1)$$

where d and a are the descending and ascending LOS measurements, respectively, at a single pixel and time step. Descending (los_d) and ascending (los_a) LOS unit vectors include only their vertical (v) and east-west horizontal (ew) components. We apply Equation 1 to estimate V and H_{ew} at each pixel and time step.

2.2. InSAR Results

We depict cumulative vertical and east-west horizontal displacements between 4 March 2015–31 March 2020 in Figures 2a and 2b, respectively. In general, the vertical component is larger than the horizontal counterpart, consistent with previously proposed mechanisms of surface displacement in this region (e.g., poroelastic fluid flow (Deng et al., 2020; Staniewicz et al., 2020) and normal faulting (Staniewicz et al., 2020)). We find that the land surface both rises and falls in the portions of the Delaware Basin where there is a high density of horizontal and disposal wells, and is relatively static elsewhere (see Figure 2b inset and horizontal well region outline in Figure 2a). We note that the deforming areas include both seismically active and aseismic areas (see Figure 1a). This spatial correlation implies that the deformation can be linked to oil and gas operations, but variations in displacement patterns suggest that, depending on the region, different mechanisms may be dominating, which may explain the occurrence or absence of seismicity.

In Figure 2c, we modified the scale for cumulative vertical displacement to highlight narrow, short-wavelength linear deformation features in the southern portion of the basin, below the Grisham Fault. These features strike northwest-southeast with a gradual clockwise rotation to the south. In contrast, displacements north of the Grisham Fault have longer spatial wavelengths and no apparent preferred orientation. The horizontal deformation shows a similar regional distinction. To the north of the Grisham Fault, horizontal displacement magnitudes are only up to ~1/2 of the associated vertical magnitudes, but usually <1/4, and form appropriately oriented pairs of east-west displacement around subsidence and uplift features (e.g., westward motion on the right and eastward motion on the left of a subsidence bowl). Below the Grisham Fault, horizontal displacements are typically 1/2 to 3/4 of the associated vertical displacements (in some instances the horizontal even exceeds the nearby vertical), the preferred orientation of features is northwest-southeast, and there are fewer pairs of horizontal displacements around strong subsidence features. Thus, surface deformation in the zones to the north and south of the Grisham fault apparently respond differently to industrial operations.

The outlined subregion in Figure 2c corresponds to the highest density of seismic activity in the southeastern quadrant of the basin (Figure 1a), suggesting that the linear InSAR displacement features could be related to the earthquakes. In Figure 3, we display the subregion from Figure 2c to compare these linear features with the tectonic stress field (Figure 2a) and seismicity from the TexNet catalog (Figure 2b). Lund Snee and Zoback (2018) compiled measurements of maximum principal horizontal stress (S_{Hmax}) orientations, depicted as red lines in Figure 2a, and ranked their quality based on the number, depth range, and agreement of measured stress indicators (the authors consider only orientations with A-C ranking sufficiently robust for plotting and analysis). The highest-quality S_{Hmax} orientations ("A" and "B" lines) are parallel to the linear deformation features. As shown in Figure 2b, seismicity also tends to align with the InSAR deformation patterns. All three data sets independently display the same rotation in strike from ~300° in the northwest corner of the subregion to ~330° in the southeast. Lund Snee and Zoback (2018) classify the stress state of the Delaware Basin as a predominantly normal-faulting regime. Under these stress conditions, normal faults striking parallel to S_{Hmax} are the most-susceptible to fail. Thus, the spatial relationship of these three data sets suggests that slip on pre-existing normal faults is a potential mechanism for the observed deformation in the southeastern zone of the Delaware Basin.

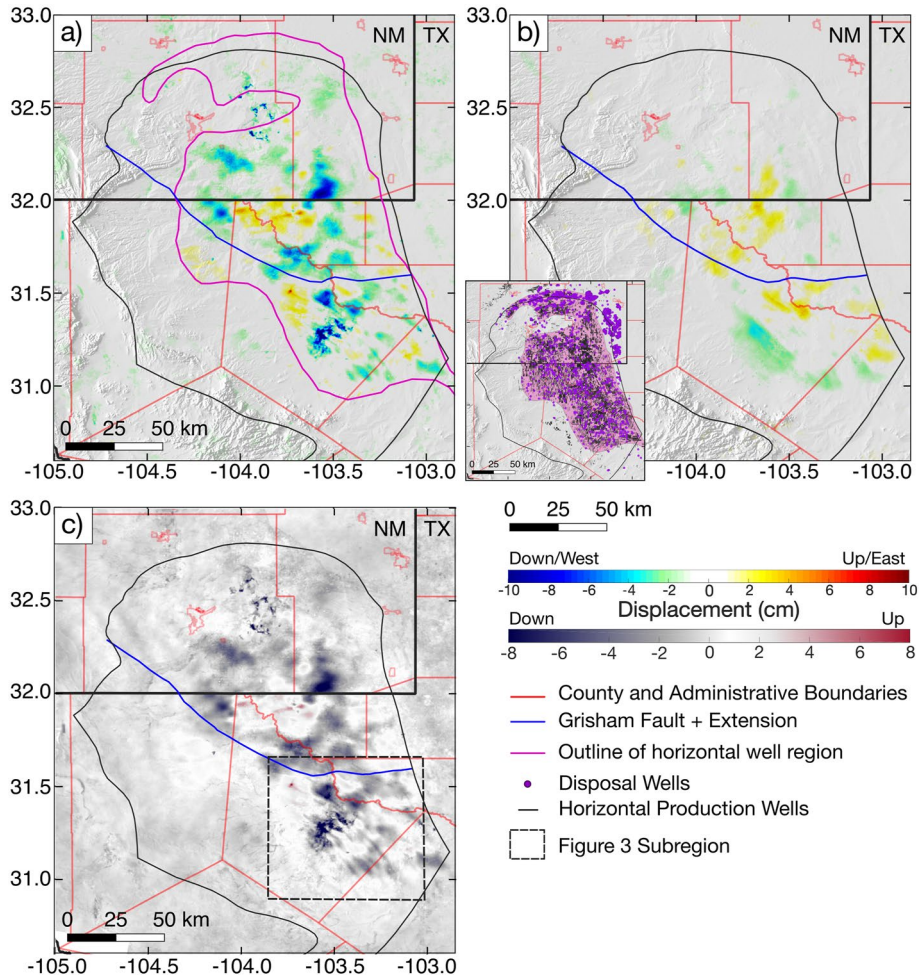

Figure 2. InSAR results in the Delaware Basin. (a) vertical and (b) east-west horizontal cumulative displacement between 4 March 2015–31 March 2020. In (c), We modified the color scale of the vertical displacement to highlight the linear features in the southeastern portion of the basin. Vertical displacements north of the Grisham fault and its extension have longer wavelengths and no preferred orientation. In (a) and (c), warm colors are uplift and cool colors are subsidence, whereas in (b), warm colors indicate eastward motion and cool represent westward. The inset in (b) shows the locations of disposal and horizontal production assigned to the Delaware Basin. The outline containing the region with a high density of horizontal wells is in pink, which is also included in (a) for reference; there is little measured deformation outside this region.

2.3. Choice of Modeling and Study Area

We use an Okada edge dislocation analytic model (Okada, 1985) to test the hypothesis that normal fault slip is the source of linear deformation features in the southeastern zone of the Delaware Basin. In this model the surface displacements are caused by a slipping plane contained within a homogeneous, elastic half-space. Comparing such a fault model with the InSAR displacement field will indicate whether fault slip is a plausible mechanism for the expected i) geometry and location of the planes, and ii) range of slip magnitudes. These model results, however, need to make sense in the larger geophysical context, including the earthquake depths, focal mechanisms, and the spatial relationship of these earthquakes to the deformation. Therefore, to define a suitable study area, we identified a region satisfying the following criteria:

1. A simple, yet distinct, deformation feature with a clear preferred orientation in vertical and east-west horizontal InSAR components
2. Sufficient seismic station coverage to provide accurate focal depths
3. Earthquakes large enough to determine focal mechanisms ($M_{W>}$ ~3)
4. Deep wells with sonic logs to define the local geologic and velocity structure

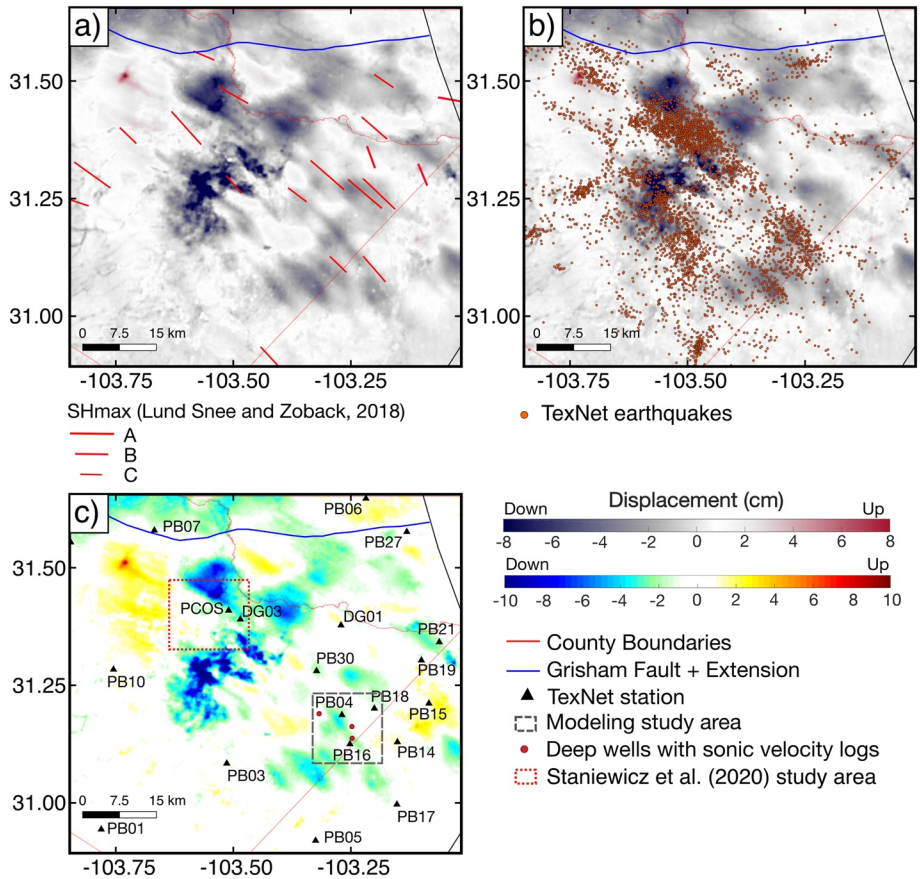

Figure 3. Subregion with saturated color scale comparing linear deformation features to (a) S_{hmax} orientations (Lund Snee & Zoback, 2018) and (b) TexNet events. In (a), the quality of S_{Hmax} measurement is indicated by the length of the vector, where "A" is the highest quality, "B" is good, and "C" is moderate. We exclude lower-quality measurements from our analysis. (c) Shows the subregion with normal color scale. Our study area is the gray, dashed box, with four TexNet stations (black triangles) near moderately-sized earthquakes. Deep wells with sonic logs used to create the 1D velocity model are the red dots.

The first criterion defines the characteristics of the deformation feature we seek to reproduce using Okada edge dislocations. The latter three criteria address the required accuracy for the earthquake data, if we are to compare the deformation modeling results to seismicity.

The study area we selected is outlined by the dashed gray box in Figure 3c. Although there are larger deformations elsewhere nearby (Staniewicz et al. (2020) modeled the area outlined in red), the area we have selected contains a relatively isolated, clear linear feature that exhibits both vertical and east-west horizontal components (Figures 4a and 4b, respectively) in the InSAR measurements, and aligns well with both seismicity from the TexNet catalog and the S_{Hmax} direction. However, the local wells show poor spatial correlation with the expected deformation from fluid volume and pore pressure changes. For example, as described in Text S2 and depicted in Figure S7 in Supporting Information S1, there are few production wells (oil or groundwater) collocated with the observed subsidence along the linear feature of interest, and there is little-to-no uplift near active disposal wells. Therefore, explaining this deformation feature needs geomechanical mechanisms other than (or in addition to) radial changes in fluid volume. Also of note is that our selected study area coincides with the region identified by Teng and Baker (2020) as having the highest seismic hazard in the Delaware Basin. Thus, it is a region of particular importance for operation managers to understand.

We present the related seismic analysis in a companion paper by Sheng et al. (2022a). In our study area, they determined moment tensors for nine events (Table 1) along with the relocation of numerous smaller earthquakes. This analysis used sonic logs from three deep wells in our study area (red circles in Figure 3c) to develop the

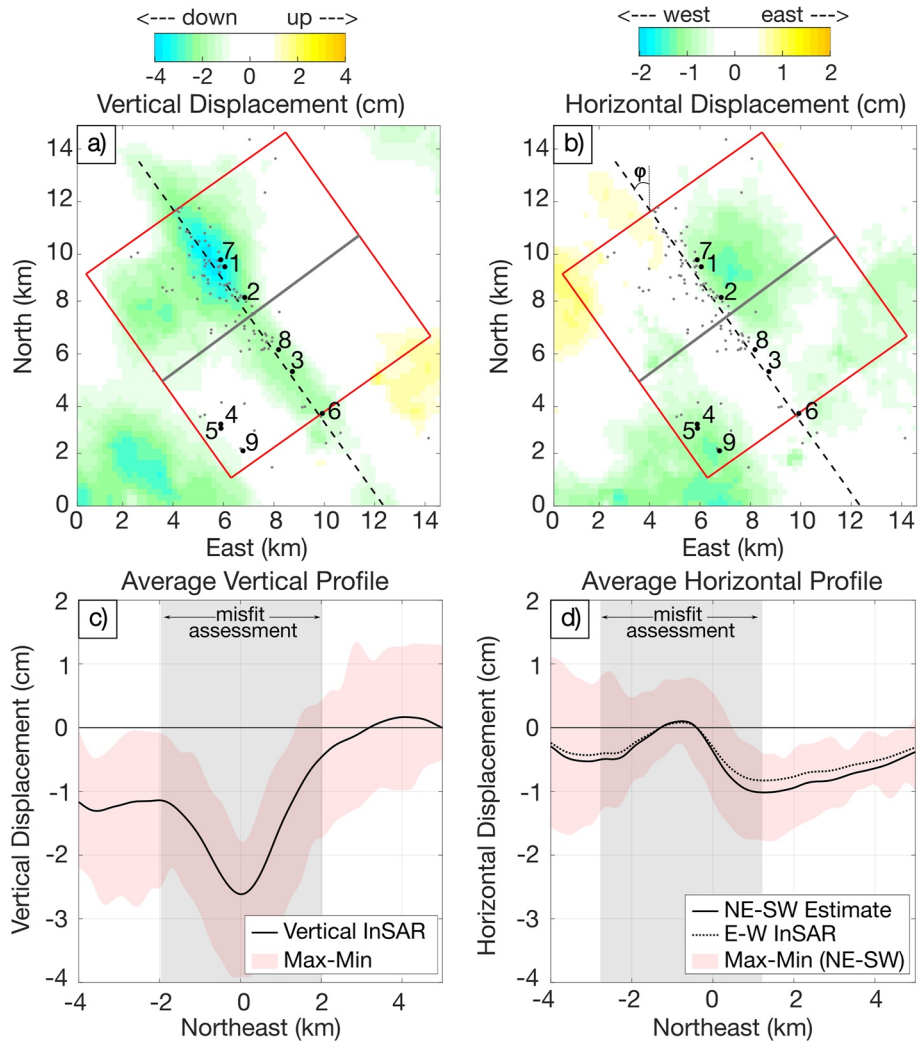

Figure 4. interferometric synthetic aperture radar (InSAR) results in selected study area. (a) Vertical and (b) east-west horizontal cumulative InSAR deformation, with relocated moment tensors (black, numbered dots) and earthquakes (gray dots). Within the red boxes, we calculated the average vertical and horizontal profiles along the gray line, perpendicular to the midline (dashed black line), which we assume to be the azimuth (φ) of the predicted faults. The bottom panel shows (c), the average vertical profile, and (d), the average east-west horizontal and estimated northeast-southwest horizontal profiles. During modeling, we calculate the misfit within the shaded gray regions in (c) and (d).

local velocity model that tightly controls earthquake focal depth and moment tensor solutions. Earthquake focal depths concentrate between 1.5 and 3.0 km below ground level, with approximately 80% of the events located in the DMG; fewer than 2% are as deep as the Wolfcamp formation and none locate in the basement. All of the moment tensor solutions are consistent with normal faulting on high-angle planes striking northwest-southeast, with the dip direction split almost evenly between northeast and southwest dips (Table 1). Sheng et al. (2022a) also found no spatiotemporal correlation between fracked wells and the earthquakes, suggesting that they were not induced by hydraulic fracking; rather, they need to be explained by another driving mechanism, such as wastewater disposal, oil and gas production, or perhaps a combination of the two.

Hypocenters determined by Sheng et al. (2022a) align with the linear deformation feature in our study area, as shown in Figures 4a and 4b. The dashed black line delineates the midline of the displacement feature of interest for initial analysis. Epicenters of the nine events with moment tensors are the numbered black dots, whereas smaller earthquakes determined through conventional location analysis are the gray dots. Earthquakes numbered 1–3 and 6–8 lie along the midline, thus we define them as Group 1, and the relocated smaller earthquakes are densely packed around the same feature. Events 4–5 and 9 (Group 2) form a smaller linear trend to the southwest

Table 1
Moment Tensor Solutions (Adapted From Sheng et al., 2022a)

ID#	Focal depth (km)	Strike	Dip	Rake	M_w
1	2.4 ± 0.1	152	82	−77	2.95
2	1.8 ± 0.2	146	68	−80	2.90
3	2.0 ± 0.2	150	70	−82	2.70
4*	1.4 ± 0.1	326	75	−83	2.84
5*	1.4 ± 0.1	327	74	−82	3.18
6	1.6 ± 0.2	326	70	−81	2.89
7	1.6 ± 0.1	336	63	−76	3.18
8	2.0 ± 0.1	166	81	−65	2.81
9*	1.6 ± 0.1	338	68	−78	2.76

Note. Stars indicate the earthquakes that belong to group 2; the others belong to group 1. All solutions strike sub-parallel to one another and have predominantly dip-slip motion.

of the midline, but striking in the same azimuthal direction. In addition, the strikes of the moment tensor solutions are sub-parallel to the azimuth of the midline and earthquake location trends, with predominantly normal slip. We now need to determine whether fault slip can also explain the deformation, if it is consistent with the seismicity, and how it might be related to oilfield activity. The remainder of this paper is devoted to answering these questions.

3. Okada Edge Dislocation Modeling

3.1. Methods

We model surface deformation due to slip on normal faults using Okada edge dislocations (Okada, 1985), using the dmodels Matlab package (modified for ease of use with our data formats) from Battaglia et al. (2013). As shown in Figure 5, the basic 2D model is a plane of infinite length (extending into the page), parameterized by the dip direction and angle (θ), and depths to the top and bottom edges (d_t and d_b, respectively), contained within an elastic half-space. In our approach, X is the lateral distance between the midline at x = 0 and the top edge of the fault, and s is the magnitude of slip in the down-dip direction. This 2D analytical model of surface deformation consists of only two components: vertical and fault-perpendicular horizontal. When extended to the 3D analytic model, the edge dislocation is a plane of finite length (L) and the surface deformation includes vertical, eastward, and northward components of motion. Due to the limitations of polar orbital paths, InSAR is less sensitive to northward motion, and we exclude this component from our modeling.

3.1.1. 2D Modeling

We use the 2D model to constrain the approximate depth intervals of slip by comparing forward models of Okada edge dislocations to the measured InSAR data using a parametric sweep. Our initial assumption is that the linear feature of interest can be explained by a single infinitely long fault plane oriented parallel to the midline in Figures 4a and 4b. However, the study area undoubtedly consists of multiple deformation sources in addition to a single slipping fault which dominates the signal. In order to reduce the sensitivity of our analysis to these other sources, we created an average InSAR profile parallel to the solid gray line in Figures 4a and 4b, using data from within the red boxes. The resulting profiles are shown in Figures 4c and 4d. In (c), the vertical profile is the black line; however, in (d), the average east-west displacement depicted by the dashed black line is not strictly fault-perpendicular, as required in the data for the 2D modeling. It is not possible to determine the true northeast-southwest deformation from only two InSAR components; however, if we assume that the measured displacements along the linear feature are due to pure dip-slip motion on a fault parallel to the midline, then there is a unique solution to the required northeast-southwest displacements (H_{ne-sw}) via the trigonometric relationship in Equation 2:

$$H_{ne-sw} = \frac{H_{e-w}}{\cos\varphi}, \tag{2}$$

where H signifies horizontal motion and subscript e-w indicates east-west motion. Variable φ is the angle between North and the strike of the midline (35.3°), as shown in Figure 4b. The resulting fault-perpendicular displacement profile is the solid black line in Figure 4d. In our model, we use the vertical and estimated northeast-southwest horizontal profiles as the reference data for misfit assessment within the gray regions in Figures 4c and 4d. The chosen regions in each profile have the same number of measurements (n), but are offset from each other, such that the area in vertical is centered around the valley at 30 m and in horizontal is centered around the peak at −777 m. Beyond these regions, the InSAR profiles deviate from the expected deformation due to a single edge dislocation and are more likely to be influenced by other sources.

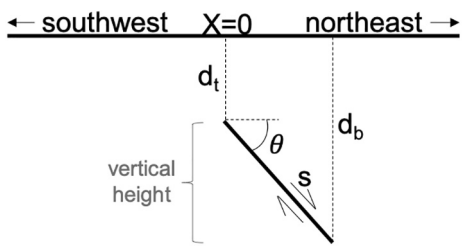

Figure 5. Schematic diagram of the fault geometry for a 2D edge dislocation in a homogeneous elastic half-space. In 3D, the predicted fault strikes northwest, thus the fault-perpendicular profile is in the northeast-southwest direction. Fault parameters are described in Table 2; we define the vertical height as the distance between the top and bottom edges of the fault in depth.

Table 2
Parameter Space for 2D Edge Dislocation Models

Parameter	Values	Notes
Dip direction	northeast or southwest	Strike parallel to midline (dashed line in Figures 4a and 4b)
Dip magnitude (θ)	5–90 (°)	θ is an integer
Depth to top edge (d_t)	100, 200, …, 6,300 (m)	
Depth to bottom edge (d_b)	200, 300, …, 6,400 (m)	$100\ \text{m} \leq (d_b - d_t) \leq 6{,}300\ \text{m}$
Location of top edge (X)	–	Determined from vertical model and InSAR
Poisson ratio (υ)	0.25	Kept constant

In the parametric sweep, we assess the fit of all forward Okada edge dislocation models characterized by the parameter sets developed from the values listed in Table 2. We selected a common value for the Poisson ratio (0.25) and kept it constant during modeling to simplify the parameter space. We determine the X-location for the top edge of the fault relative to the midline (x = 0) directly from the model: for a given parameter set i consisting of d_t, d_b, θ, and dip direction, we compute the vertical forward model of the dislocation with the top edge at x = 0 and 10 cm of normal slip, and then adopt the lateral offset between the minima in the vertical forward model and InSAR profile as the appropriate X-location.

With the full geometry for parameter set i defined, we determine the magnitude of slip (s) best-fitting the InSAR profiles by minimizing a modified RMS error (E), which we refer to as misfit, as defined in Equation 3:

$$E_i = \sqrt{\frac{\sum_{i=1}^{n} \left((\hat{\upsilon}_i - (\upsilon_i + \mathrm{DS}_{\upsilon_i}))/2\right)^2 + \left(\hat{h}_i - (h_i + \mathrm{DS}_{h_i})\right)^2}{2n}}. \quad (3)$$

Here, $\hat{\upsilon}$ and $\hat{h}$ are the vertical and horizontal displacements, respectively, from the forward model, the un-hatted υ and h are from the InSAR profiles, and n is the number of samples in the InSAR profile, within the misfit assessment bounds. Since our main goal in the 2D modeling is to fit the wavelength and relative amplitudes of the vertical and horizontal data, we allow datum shifts in each (DS_υ and DS_h, respectively) during measurement of the misfit, such that the minima in vertical and maxima in horizontal between the forward model and data are equal (see Figure S10 in Supporting Information S1). We also weight the vertical differences by 1/2 in order to account for the higher amplitude in vertical motion compared to horizontal and better allow the latter to influence the solution. We prefer this weighted misfit assessment because a dip-slip edge dislocation results in vertical displacements that are approximately twice the amplitude of the horizontal, within our chosen misfit bounds, which is also the proportion observed in the InSAR profiles. Weighting the vertical differences between data and model by 1/2 results in a solution in which the proportion of differences to amplitude in each displacement component are comparable.

3.1.2. 3D Modeling

While the 2D modeling is useful for constraining appropriate edge dislocation parameters, we require the 3D model to analyze the relationship of proposed faults to the local seismicity and well locations, and better understand the deformation due to slipping faults in the context of the InSAR displacements in the full study area. Using the dmodels package (Battaglia et al., 2013), we are able to extend any of the 2D, one-fault forward models to the full 3D space by adopting the X-location and uniform slip magnitude resulting from 2D modeling, and assigning finite length L (equal to the length of the midline) and strike direction (parallel to the midline). Observations from comparing these 3D, one-fault models to the full InSAR data inform our development of increasingly complex multi-fault models.

In the first stage of multi-fault modeling, we assume uniform slip on numerous edge dislocations of varying length. After selecting the number of faults (N) to include in the modeling, we manually select the endpoints of the top edge of each, thus defining their locations in the 3D space. For simplicity, we then select and assign identical d_t, d_b, and θ to each fault plane, but permit the strikes (as determined by the endpoints) and dip direction to vary on each, noting that we do not allow significant deviations (± 10°) from the strike of the midline or linear

trends created by the moment tensor solutions from Sheng et al. (2022a). We then solve for the magnitude of uniform slip on each fault plane using the relationship in Equation 4:

$$Wd = WGs', \tag{4}$$

where d is a vector of vertical and east-west horizontal InSAR data, s' is the unknown [N x 1] vector of slip magnitude on each fault plane, and G is the Green's function matrix relating slip magnitude to vertical and east-west horizontal surface deformation at each pixel, via the Okada (1985) equations. Matrix W is a diagonal weighting matrix that prioritizes data pixels near the fault segments. Along its diagonal is $1/R_i^2$, where R_i is the distance between data pixel i and the top edge of the nearest fault segment. We use dmodels (Battaglia et al., 2013) to generate the appropriate G matrix and apply Equation 4 to find the vector s' of uniform dip-slip magnitudes that best fits the selected InSAR data in a least-squares sense.

After developing a uniform-slip, multi-fault model, we introduce additional complexity by discretizing each plane into finite patches approximately 1,000 m in length along strike and 200 m in down-dip width. The slip vector s' is now equal in length to the number of discretized patches. Equation 4 is significantly underdetermined, leading to an unrealistically rough solution of vector s'. Therefore, for the patch model we include a smoothing operator that minimizes the 2D second-derivative of fault slip, resulting in the regularized inversion relation shown in Equation 5:

$$\begin{bmatrix} Wd \\ 0 \end{bmatrix} = \begin{bmatrix} WG \\ \alpha^2 D \end{bmatrix} s', \tag{5}$$

where α is the Lagrange operator that determines the weight put on the smoothing, and D is the second-order finite difference operator such that $\nabla^2 s' = Ds'$.

3.2. Results

3.2.1. 2D Modeling

The purpose of the 2D, one-fault modeling was to constrain the approximate depth intervals (d_t *to* d_b) of slip. As indicated in Table 2, we explored vertical slip heights (d_b–d_t) ranging from 100 to 6,300 m, contained between depths of 100–6,400 m. The chosen range of d_t and d_b approximately corresponds to the complete geologic section above the basement (Figure 1c). In our simple 2D model there are parameter trade-offs, in which some parameter sets are geologically more realistic than others, despite having similar misfit to the InSAR data. To explore these trade-offs, we condensed our parameter space to include fault width ($w = (d_b - d_t)/\sin\theta$), the approximate 2D stress drop ($\Delta\sigma_{2D} = 0.85\ \mu s/w$) (Kanamori & Anderson, 1975; Starr, 1928), and the midpoint depth of the dislocation. The 2D stress drop calculation requires knowledge of the shear modulus (μ); we used the P velocity (Vp = 4.3 km/s) and Vp/Vs ratio of 1.89 for depths between 2 and 3 km, from Sheng et al. (2022a), and a density of 2700 kg/m^3 to estimate a shear modulus of 14 GPa.

In Figure S8 in Supporting Information S1, we show the trade-offs between stress drop and fault width for subsets of southwest-dipping faults with vertical heights ranging between 100 and 1,500 m, colored by the midpoint depth range. All subsets display similar trends (e.g., greater fault widths and shallower depths require lower stress drops to fit the data). Additionally, for vertical height subsets between 100 and 1,000 m, the misfit values of the best 20% of models are virtually indistinguishable, although a further increase in vertical height gradually increases the misfit (Figure S9 in Supporting Information S1). Despite fitting the InSAR data, most stress drops for models with vertical heights of 100 m exceed 100 MPa, which is unrealistically high. For vertical heights of 500 m, the stress drops reduce to <35 MPa, and for vertical heights of 1,500 m, all explored models have stress drops <4 MPa. Although a further increase in vertical height reduces the predicted stress drops, the misfit values of the best-fitting models increase to unacceptably high levels (Figure S9 in Supporting Information S1). We thus constrain our parameter space to include only those models with vertical heights ranging between 500 and 1,500 m, to maintain a balance between plausible stress drops and model fit.

In addition to highlighting important trade-offs, Figure S4 in Supporting Information S1 shows that, in all subsets of vertical height, the best-fitting models have midpoint depths around 2200 m, regardless of fault width. While

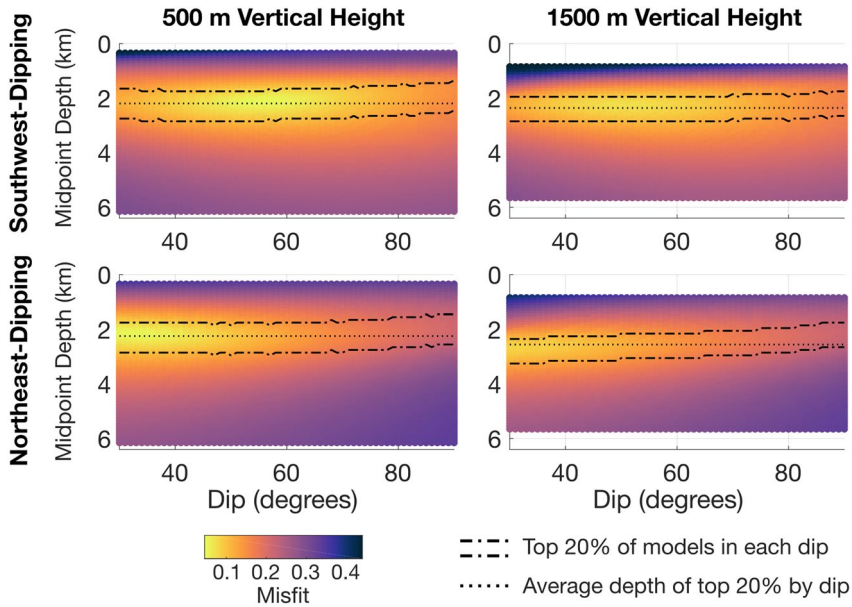

Figure 6. Misfit values for models as a function of midpoint depth, dip magnitude and direction, and vertical height. Regardless of parameter set, the top 20% of models in each integer dip bin have midpoints between ~1.5 and ~3 km. We exclude dips below 30 based on the local stress conditions (see Figure 7).

the best-fitting midpoint depth appears to be invariant to vertical heights and width, the midpoint depth also has low sensitivity to dip angle. In Figure 6, we show model subsets with vertical heights of 500 m (left) and 1,500 m (right), and with either southwest- or northeast-dip (top and bottom panels, respectively). The model misfit is shown as a function of midpoint depth and dip angle. Depending on the vertical height, the best 20% of models in each dip bin have mean midpoint depths between 1,900–2,500 m. These depths coincide with the Delaware Mountain Group, the formation in which wastewater disposal is concentrated and the majority of the earthquakes occur, suggesting a connection between fluid injection and fault movement.

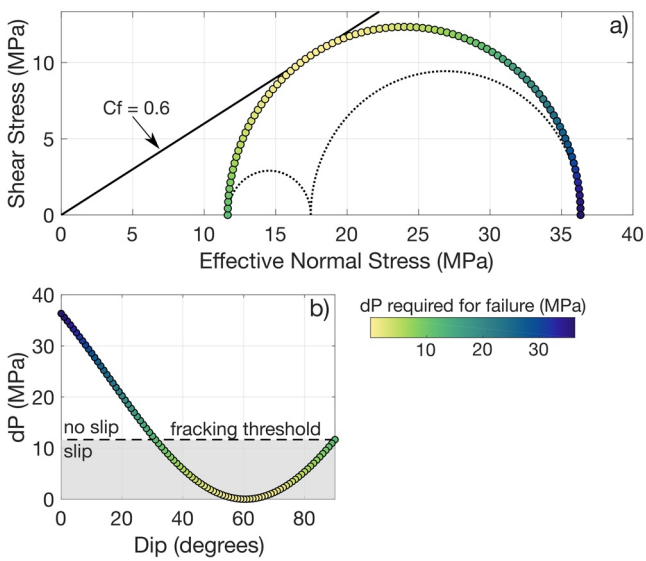

Figure 7. Minimum change in pore pressure (dP) required to reactive faults of specified dip. (a) Mohr circle and relative stresses for the Delaware Mountain group (Dvory & Zoback, 2021), assuming a coefficient of friction (Cf) of 0.6. (b) Minimum dP for slip as a function of dip. Any dP exceeding the fracking-threshold (dashed line in b) will produce new microfractures, significantly reducing the local effective stress. Thus, faults with orientations of dP greater than the fracking threshold are not expected to slip.

We are able to constrain the depth intervals and vertical heights from misfit assessment and geomechanical arguments about stress drop. We can do a similar exercise to constrain the expected dip magnitudes. Table 1 lists the high-angle moment tensor solutions from Sheng et al. (2022a), which have a median dip of 70°. For each earthquake, there exists an auxiliary low-angle plane; these low-angle planes have a median dip of 22°. Although the moment tensor analysis alone cannot distinguish between the two dips, we can eliminate the low-angle dips based on the local stress conditions. In a predominantly normal-faulting stress regime, as is the case in the Delaware Basin (Lund Snee & Zoback, 2018), low-angle faults are the furthest from failure. Figure 7 shows (a), the Mohr circle derived from measurements of the principal stress components in the southern Delaware Basin from Dvory and Zoback (2021), and (b), the minimum increase in pore pressure (dP) required for fault failure as a function of dip. Not only are low-angle faults the least likely to slip, faults with dips <30° are precluded from slipping by the local stress conditions, since the change in pore pressure required would exceed the fracking threshold (dashed line in Figure 7b) and create microfractures in lieu of fault-reactivation. Therefore, we expect to see active high-angle faults with dips >60°, consistent with the high-angle fault planes from the moment tensor solutions (Table 1).

Figure 6 shows that the best-fitting one-fault models in our constrained parameter space have dips between 30° and 40° (northwest-dipping) or 50°–60°

(southwest-dipping), suggesting that the southwest-dipping faults fit the InSAR data better under the constraint of high-angle dips. However, it is important to highlight that we allow a datum shift of the InSAR data during the misfit assessment, as demonstrated in Figure S10 in Supporting Information S1, which compares the 2D forward models of the best-fitting southwest- and northeast-dipping edge dislocations with dips of 75° and vertical heights of 1,000 m (see Table S1 in Supporting Information S1 for other parameters). The southwest-dipping fault does indeed fit the datum-shifted InSAR profiles better than the northeast-dipping example. In contrast, we note that the horizontal InSAR profile as measured (i.e., no datum shift) is better represented by the northeast-dipping fault, though there is a sacrifice in vertical fit. These results suggest an ambiguity in the dip direction for a single fault that truly best fits the InSAR data.

3.2.2. 3D Modeling

The next step is to consider slip models of finite length and uniform slip in the full 3D space. Figure S11 in Supporting Information S1 depicts the 3D finite-fault model for each 2D model from Figure S10 in Supporting Information S1. Both models reasonably reproduce the vertical subsidence along the linear deformation feature of interest, albeit with lower magnitude than the InSAR observations. In the east-west horizontal component, however, the northwest end of the midline in the InSAR data appears to be dominated by a southwest-dipping fault, whereas the southeast end may be dominated by slip on a northeast dipping fault. Therefore, we explore the possibility of a two-fault model consisting of a combination of the oppositely-dipping single-fault models from Figure S11 in Supporting Information S1. Using these observations and the expected slip interval depths constrained from the 2D model, we develop a model with two high-angle finite edge dislocations dipping toward each other in a graben structure, each with uniform slip, determined using Equation 4 (Figure S12 in Supporting Information S1). The southwest-dipping fault is rather short, but its extension along strike would contain the Group 1 earthquakes from Table 1, suggesting that the fault plane may be much longer, despite slip being concentrated in an isolated section. We thus extend each fault plane along its strike, increase the vertical width to 1,400–2800 m (to account for the range of the best 1-fault models from Table S1 in Supporting Information S1), and discretize each into multiple patches. We also include a small northeast-dipping fault parallel to the Group 2 earthquakes from Table 1. Using the regularized solution described in Equation 5, we solve for the dip slip magnitude on each patch of the three defined faults, using $\alpha = 70$ due to its position on the bend of the L-curve of the solution semi-norm versus residual norm logscale plot (Figure S13 in Supporting Information S1).

We compare the forward model of vertical and east-west horizontal surface displacements from the patched, three-fault model to the measured InSAR data in Figure 8. The top edge of each fault (F1–F3) is marked by a solid red line and its downward-looking extent is outlined by the dotted black line. The slip distributions along each fault are shown in Figure 9, where (a) depicts the bird's eye view of the average slip along each fault's down-dip direction, and (b)–(d) display the side-view of each fault from the perspective of the arrow in Figure 9a. In Figures 9c–9d, we also include the along-strike profile of modeled (black line) and InSAR (red line) surface deformation directly above the top edge of traces F2 and F3, which flank the linear deformation feature of interest. In Figures 8 and 9a, we include the locations of earthquakes from Table 1, which highlight that Group 1 falls along the trace of F3, and Group 2 aligns with F1. Therefore, in Figures 9b–9d, we show only the earthquake locations in the side-view plots for the faults with which they are associated (Group 1 in Figure 9d and Group 2 in 9b). The final detail in Figure 9 is the location of active disposal wells (gray dots), which are labeled by the volume of injected fluid in millions of barrels (MMbbl) during the time span of our study. In Figures 9b–9d, we include only the disposal wells within 2 km of the fault planes. The perforation interval of each well is indicated by the solid black lines.

The main linear deformation feature in vertical (Figure 8a) is reproduced well in the forward model (Figure 8c); likewise, the horizontal deformation from the forward model (Figure 8d) agrees with the westward sense of motion flanking the linear feature in the InSAR data (Figure 8b), without requiring a datum shift. This model, however, cannot explain the two subsidence features to the southwest of F2, nor the uplift to the southeast of F3. Consequently, there are unmodeled displacement features in the horizontal component which coincide with the same geographical areas. In Figures 9c–9d, the comparison of the model and InSAR profiles also highlight some residual deformation that has not been captured by the model. These residuals are a direct result of our decision to favor smoothly varying slip models to prevent overfitting the data with unrealistic slip distributions.

The maximum amount of slip along F1 is mostly to the northwest of the Group 2 earthquakes, all of which have a northeast dip, agreeing with the dip of F1 (Figures 9a and 9b). Although there are no large earthquakes that

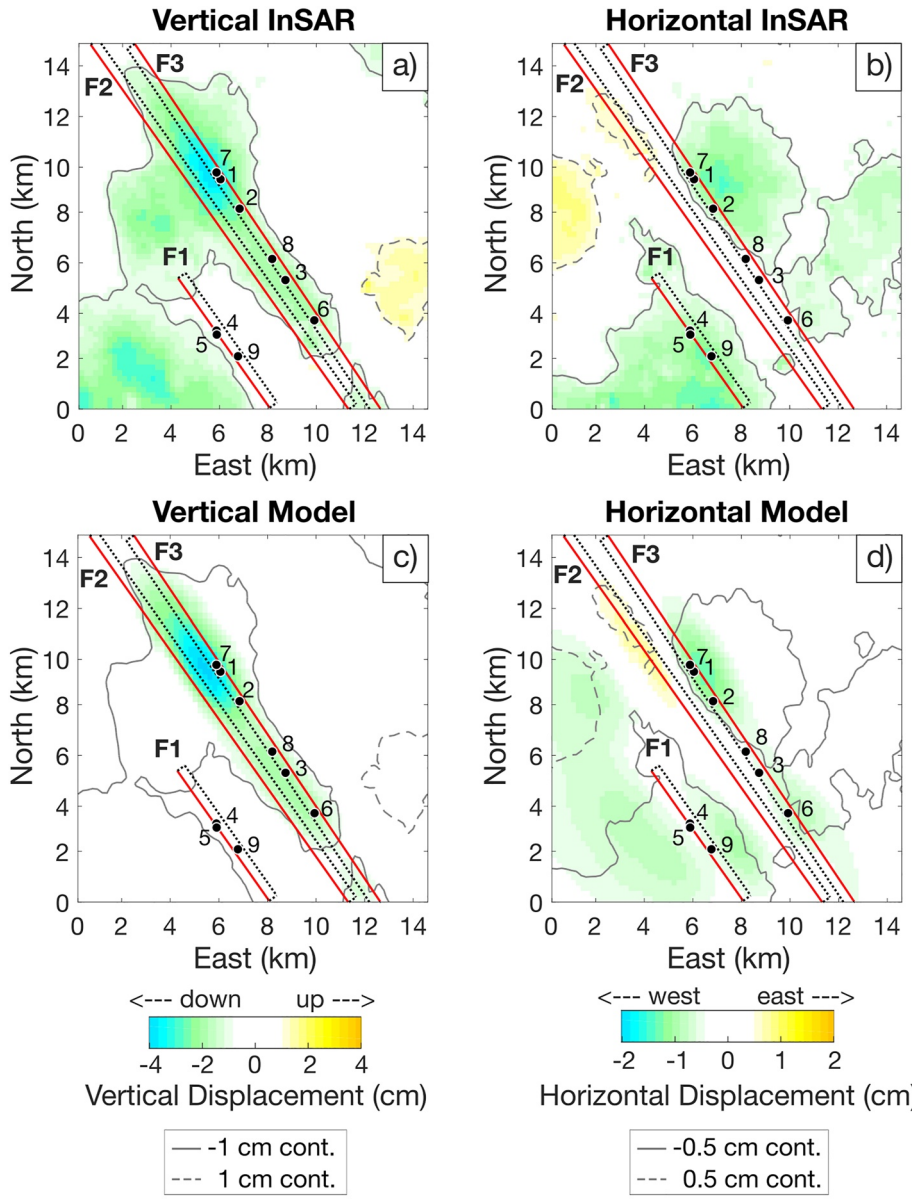

Figure 8. Three-fault model in a 3D space. The top panel is the original interferometric synthetic aperture radar data, where (a) is vertical and (b) is east-west horizontal, with gray contours highlighting major features in order to better compare with the forward model in the lower panel, where (c) is the vertical forward model and (d) is the horizontal forward model. The two edge dislocations are represented by the red lines (top edge of fault) with map-view extent depicted by the dotted lines. The gray solid and dashed shapes highlight the displacement contours.

spatially locate along the trace of F2, this fault has the greatest slip magnitude (25 cm) and extent of slip, as shown in Figures 9a and 9c. The majority of slip along F3 is confined between earthquakes #2, #7, and #1, and there is a small amount of slip (~7 cm) near earthquakes #8 and #3. We note, however, that the dip for earthquakes #6 and #7 are northeast, suggesting that they may belong to F2 or an additional unmodeled fault within the graben structure. In the former case, both northeast-dipping earthquakes would locate above the two local slip maxima on F2, whereas the latter case requires further modeling to draw any conclusions regarding the relationship to slip. The largest earthquakes do not collocate directly with the patches hosting the greatest predicted slip magnitudes, suggesting that the faults are principally slipping aseismically. Additional evidence stems from the timing of earthquakes #6–9, which all occurred after the end of the InSAR study period (post-March 2020). Thus, the

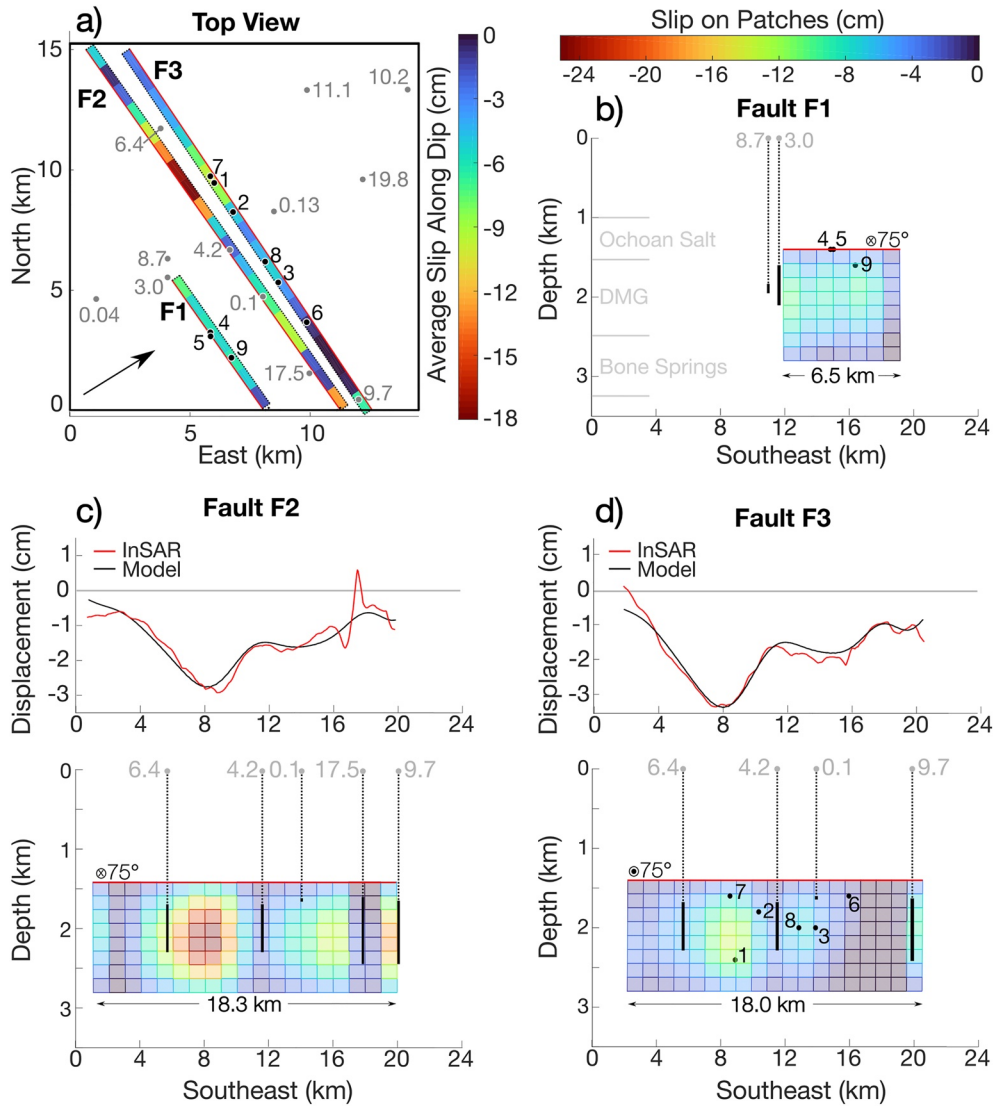

Figure 9. Slip distribution on the three-fault edge dislocation model. The top view in (a) shows the spatial relationship of the faults with the earthquake moment tensors (black dots) and disposal wells (gray dots). The numbers that accompany disposal wells are the values of cumulative injection volume between March 2015–March 2020, in millions of barrels (MMbbl). Plots (b)–(d) show the side view of each fault from the perspective of the black arrow in (a). Faults F2 and F3 (c and d, respectively) also display the InSAR and model surface deformation directly above the top edge of each respective fault. Earthquake moment tensors and disposal wells within 2 km of each fault are included in plots (b)–(d). Formation intervals are also indicated on the cross-sectional profiles in (b).

observed slip only has the potential to be attributed to earthquakes #1–5, which have a peripheral relation to the greatest slip magnitudes.

While the majority of proposed slip cannot be attributed to the earthquakes, the regions of large slip along each fault trace do coincide with the location of disposal wells. In Figures 9b–9d, local areas of maximum slip lie between adjacent disposal wells. For instance, the patches of maximum slip on F2 lie between wells with disposal volumes of 6.4 and 17.5 MMbbl, with the absolute maximum falling directly between wells with 6.4 and 4.2 MMbbl. Even on F3, where the maximum slip also lies adjacent to the well with 6.4 MMbbl, there is an observable increase in slip at the right edge of the fault that coincides with the well with 9.7 MMbbl of injection volume. Consequently, there is evidence for a link between fault slip and fluid injection in our study area.

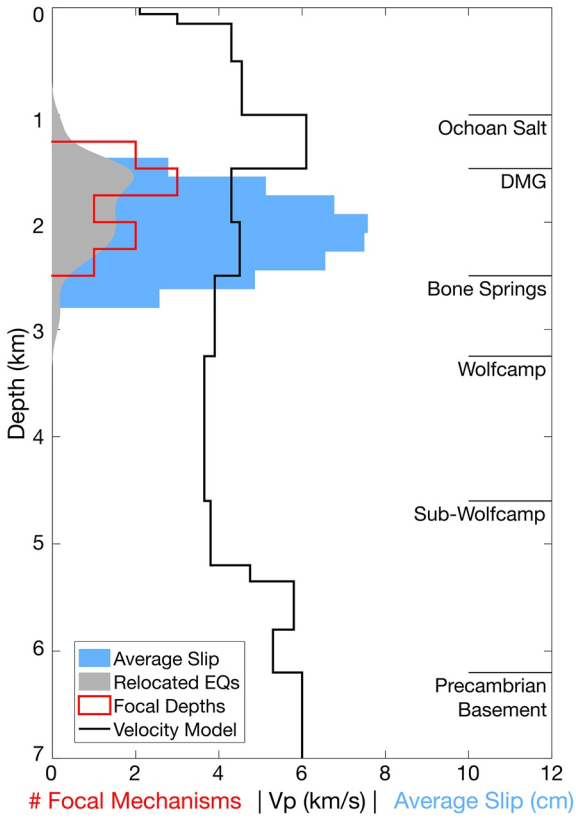

Figure 10. Summary of slip intervals from Okada modeling compared to the relocated earthquake depths (Relocated EQs), moment tensor centroid depths (Focal Depths), and velocity model from Sheng et al. (2022a). All fault motion (seismic and aseismic) extends through the Delaware Mountain group (DMG), the main formation used for wastewater injection. We developed the local formation intervals using the average depth of each formation surface (Enverus, 1999) within our study area.

Although the spatial relationship between fault slip and disposal is clear, there does not appear to be a direct correlation between the amount of slip and disposal volumes. However, there are many other variables to consider, including disposal rate, distance from the fault, and hydraulic and frictional properties of both the fault and surrounding subsurface medium. We note that the vertical InSAR profile along F2 (Figure 9c) shows signs of uplift directly above the disposal wells with the largest injection volumes, suggesting that the measured deformation may be due to the combination of many effects. In this case, it appears that injection-related uplift is superimposed on the subsidence signal from fault slip. The combined effects pose a challenge for isolating the true magnitude of slip on each fault patch. For example, on fault F2 near the disposal well with 17.5 MMbbl injection volume, there is a distinct column of little fault motion interrupting an otherwise smooth slip distribution on either side. It is possible that uplift related to the injection wells is causing an underestimation of the slip magnitudes, at this location and near other disposal wells along the fault traces.

4. Discussion

Our 2D and 3D edge dislocation model results show that the observed InSAR surface deformation can in part be explained by slip on high-angle normal faults within the DMG, with possible extension into the overlying Ochoan salts and underlying Bone Springs. In our small study area, our model consists of a long, shallow graben structure, and at least one other fault plane approximately 3–4 km to the southwest of the graben. Although there have been no detailed structural analyses in our study area, recent studies using 3D seismic arrays have mapped similar graben structures throughout Reeve's county (Charzynski et al., 2019; Hennings et al., 2021). All occurrences show graben structures mainly spanning the DMG, with slight extension into the Ochoan and Bone Springs. The grabens are all high-angle, ~0.25–1 km wide (as measured by their top edges), and spaced 2–4 km apart. The three-fault model we developed has identical characteristics, suggesting it is a part of this larger graben network. The graben features align with the modern state of stress (Hennings et al., 2021; Lund Snee & Zoback, 2018) and are consisitent with the stress state of the regional basin and range extensional episode in the middle to latest Miocene (Charzynski et al., 2019). However, there have been multiple extensional and contractional events since the formation of the basin during the Mississippian through the Permian (Hennings et al., 2021, and references therein).

The occurrence of deformation and the improved focal depth analysis from Sheng et al. (2022a) highlight that these shallow grabens are not only present, but also active. In Figure 10, we have summarized the depth distribution of average slip (blue histogram), moment tensor centroids (red histogram), and relocated earthquake hypocenters (gray histogram), along with the 1D geological model Sheng et al. (2022a) developed from the P-wave velocity profile (black line). All data peak at a depth of ~2000 m in the middle of the DMG, which hosts all the local wastewater disposal. Not only do these data fall within the same formation, they have strong spatial relationships to one another. We were able to develop a discretized fault model that aligns with the larger earthquakes in our study area and agrees with the moment tensor solutions in terms of high-angle dip, as suggested by the local stress conditions, and sense of predominantly dip-slip motion. Furthermore, though we did not constrain our model with the available well data, wastewater disposal wells are located near patches of greatest slip on each fault. Therefore, it seems likely that the nearby fluid injection is activating these normal faults; however, the displacement is clearly not all seismic.

We calculate the cumulative geodetic moment along the patched surfaces of all three faults F1–F3, using equations for seismic moment:

$$M_0 = \mu A S, \tag{6}$$

where μ is the shear modulus (we use a density of 2000 and 2700 kg/m^3 to calculate a reasonable range of shear moduli between 10 and 14 GPa), A is the rupture area, and S is the average slip. To convert seismic moment (M_0) to moment magnitude (M_W), we use the definition from Hanks and Kanamori (1979) with M_0 in Newton-meters:

$$M_W = \frac{2}{3}\left(log_{10} M_0 - 9.1\right). \quad (7)$$

The combined equivalent magnitude released during slip on all patches ranges between $M_W = 4.9$ to $M_W = 5.05$, whereas the combined equivalent magnitude of all earthquakes recorded by the TexNet array (between 01 January 2017 to 31 March 2020) in our study area is $M_W = 3.9$. Hence seismicity accounts for only 1.8%–2.5% of the predicted fault slip. If normal slip is contributing to the InSAR observations, as suggested by our model, it is predominantly aseismic.

To date, the role of aseismic slip in induced seismicity has been largely limited to indirect inference and associated with hydraulic fracturing (Cornet et al., 1997; Eyre et al., 2019, 2020; Guglielmi et al., 2015; Zhu et al., 2020), so the implications of its occurrence in the Delaware Basin are challenging to know. Though Sheng et al. (2022a) and our work suggest that wastewater disposal is likely inducing seismic and aseismic slip on normal faults in the DMG, it is unclear whether both are a direct consequence of the fluid injection, or whether aseismic slip triggers seismic events and/or vice versa. Based solely on our static 3D model, it is clear that the largest earthquakes along F1 and F3 do not coincide with the patches hosting the largest cumulative displacements (up to 25 cm), but rather are located around the periphery in patches with slip <12 cm. This suggests that hydraulic and frictional conditions vary along the faults.

Although our focus here has been on a small area in the Delaware Basin, we can extend our findings to the rest of the basin, which has contrasting deformation and seismicity patterns between the southern and northern sections. As demonstrated in the full-basin InSAR results (Figure 2), the linear deformation features only occur where there is seismic activity, suggesting that aseismic and seismic slip are intimately linked. Thus, the lack of seismicity and linear deformation features to the north of the Grisham fault could indicate that favorably oriented normal faults in the DMG are absent. However, this explanation lacks supporting evidence and is rather ad hoc. Dvory and Zoback (2021) analyzed the stress state and frictional stability of faults in the basin. They found that the fluid pressure in the DMG in the northern portion of the basin was diminished by conventional oil and gas production in that formation in the decades before unconventional exploitation began. Under this explanation, pressures are currently too low to induce fault slip, even under conditions of wastewater injection in the presence of favorably oriented faults. In contrast, Dvory and Zoback (2021) found that the stress state is near-critical south of the Grisham fault, where very little production has occurred in the DMG. Thus, a modest pressure rise of a few MPa due to wastewater disposal in the DMG would bring favorably-oriented normal faults to failure, both seismically and aseismically. However, we note that not all of the observed deformation in the southeastern portion of the basin may be attributed to fault motion. There is evidence that fault slip is prevalent along the main subsidence feature in the study area investigated by (Staniewicz et al., 2020; Figure 3c), despite having a shape that is only sharply linear on the southwestern edge (though some of the subsidence associated with this feature may be due to horizontal production). On the other hand, the strong subsidence signals to the south of their study area (approximately longitudes −103.6 to −103.4 and latitudes 31.1–31.3) have wavelengths and magnitude that may be more consistent with shallow production, such as groundwater withdrawal used for hydraulic fracturing. It is also possible that some of the linear features in the southeastern basin are due to faults acting as hydraulic barriers to cross-flow, which may cause asymmetric deformation in the presence of nearby pumping or disposal. While the occurrence of seismicity along these features suggests at least some degree of fault motion, it may be a combination of these deformation mechanisms that are highlighting fault traces in this region.

Consequently, one limitation of our model is the assumption that the observed surface deformation is due exclusively to fault slip. More likely it results from the combined effects of fault slip (both seismic and aseismic), oil and gas production, wastewater and CO_2 injection, and groundwater pumping for municipal, agricultural, and industrial purposes. Further evidence for multiple causes is clearer in the northern portion of the basin where there is observable deformation but no obvious patterns suggestive of fault movement. The contribution of other deformation sources within our own study area are clear in Figures 9c and 9d, where the smoothed slip model has up to 2 cm of misfit to the InSAR data, suggesting additional mechanisms contribute to the surface displacement. In particular, there is less subsidence in the InSAR data than predicted near some disposal wells, suggesting uplift

from fluid injection. If the latter contributes to surface deformation, then we cannot rule out production-related subsidence as well, especially from shallow groundwater wells. Staniewicz et al. (2020) addressed the possibility of multiple deformation sources by removing the predicted vertical deformation from normal fault motion and computing residual vertical displacements resulting from subsurface volume changes. While forming a useful approach for modeling volumetric changes from fluid extraction and injection, including these in our model would not change our primary conclusion that high-angle normal faults in the DMG are moving.

It is essential to highlight the importance of including both InSAR components in the development of our model. The observations we made about the east-west horizontal deformation patterns produced from the single faults in Figure S7 directly guided us to the two-fault graben structure in Figure S8, both in Supporting Information S1. In addition, faults F1 and F3, which we in part defined to align with the focal depths and sense of slip of the nine larger earthquakes, cannot reproduce the observed InSAR deformation without the inclusion of fault F2. Had we used only the vertical deformation in the development of our model, we would have lacked the information needed to determine the geometry of all three faults, which altogether create a consistent story with the additional geophysical data available and recent works showing shallow graben structures in the DMG (Charzynski et al., 2019; Hennings et al., 2021).

5. Conclusions

Our InSAR analysis shows a stark contrast in deformation patterns between the northern and southeastern portions of the Delaware Basin. The three-fault model we developed from both components of these InSAR data suggests that fault motion is responsible for the linear deformation features in the southeastern portion of the Delaware Basin. Based on the spatial relationship between wastewater disposal wells, critically stressed faults, and relocated earthquakes, we have shown that wastewater injection in the DMG has likely been inducing both aseismic and seismic fault movement in this area. However, it remains unclear whether the aseismic slip and seismic events are both a direct result of pore pressure increase, or if induced aseismic slip triggers the seismicity or vice versa. Theoretical numerical modeling of injection-induced aseismic slip will be paramount to understanding the complex subsurface response to wastewater disposal, and our work provides observation-based slip models that can be used to constrain and contextualize these efforts. As we continue to explore the evidence for aseismic slip in the rest of the southern Delaware Basin and determine the likely geomechanical mechanisms contributing to deformation in the northern portion of the basin, it may be possible to constrain the conditions that lead to aseismic and seismic slip, so operators can better plan the location and operating standards for future wells.

Data Availability Statement

The InSAR cumulative displacements (vertical and east-west horizontal) are available in data citation: Pepin et al. (2021) via https://doi.org/10.5281/zenodo.5842110. The relocated earthquakes and moment tensor solutions data set (Sheng et al. (2022b)) from Sheng et al. (2022a) can be found at https://doi.org/10.5281/zeenodo.5841588. The edge dislocation modeling software we used for this research is available in Battaglia et al. (2013) via download at https://pubs.usgs.gov/tm/13/b1/. The InSAR single-look-complex images for all orbits are available in: ASF DAAC (2014-2020). Users must register for a free Vertex account to access data. The TexNet data and station information are available in this in-text citation reference: Savvaidis et al., 2019. The USGS Earthquake Catalog can be found in U.S. Geological Survey, Earthquakes Hazard Program (2017). The industry well data and subsurface formation surfaces supporting this research are available via Enverus' (previously Drillinginfo) online database (Enverus, 1999). This database requires a paid subscription and is not available to the general public. Groundwater well data supporting this research is available for free via the Texas Water Development Board in their Groundwater Database (GWDB) and Brackish Resource Aquifer Characterization System (BRACS) Database via data citation: Texas Water Development Board (2013). The data on stress orientations and local stress are included, respectively, in these papers: Lund Snee & Zoback, 2018 and Dvory & Zoback, 2021.

Acknowledgments
This work was supported by the Stanford Center for Induced and Triggered Seismicity (SCITS) and the Department of Energy (Basic Energy Sciences; Award DE-SC0020445). The authors report no conflicts of interest pertaining to this work.

References

ASF DAAC. (2014-2020). *Contains modified Copernicus Sentinel data 2014-2020, processed by ESA. Vertex data search*. Retrieved from https://search.asf.alaska.edu/#/

Battaglia, M., Cervelli, P. F., & Murray, J. R. (2013). A MATLAB software package for modeling curstal deformation near active faults and volcanic centers. *Journal of Volcanology and Geothermal Research*, *254*, 1–4. Retrieved from https://pubs.usgs.gov/tm/13/b1/

Berardino, P., Fornaro, G., Lanari, R., & Sansosti, E. (2002). A new algorithm for surface deformation monitoring based on small baseline differential SAR interferograms. *IEEE Transactions on Geoscience and Remote Sensing*, *40*(11), 2375–2383. https://doi.org/10.1109/TGRS.2002.803792

Charzynski, K., Faith, K., Fenton, Z., Shedeed, A., McKee, M., Bjorlie, S., & Richardson, M. (2019). *Delaware basin horizontal Wolfcamp case study: Mitigating H2S and excessive water production through isolating densely fractured intervals correlative to seismically mapped shallow graben features in the Delaware mountain group*, SEG Global Meeting Abstracts. (pp. 4126–4141).

Chen, C. W., & Zebker, H. A. (2001). Two-dimensional phase unwrapping with use of statistical models for cost functions in nonlinear optimization. *Journal of the Optical Society of America*, *18*(2), 338–351. https://doi.org/10.1364/josaa.18.000338

Cornet, F. H., Helm, J., Poitrenaud, H., & Etchecopar, A. (1997). Seismic and aseismic slips induced by large-scale fluid injections. In S. Talebi (Ed.), *Seismicity associated with mines, reservoirs and fluid injections* (pp. 563–583). BirkhäuserPageoph Topical Volumes. Retrieved from https://doi-org.stanford.idm.oclc.org/10.1007/978-3-0348-8814-1_12

Deng, F., Dixon, T., & Xie, S. (2020). Surface deformation and induced seismicity due to fluid injection and oil and gas extraction in western Texas. *Journal of Geophysical Research: Solid Earth*, *125*(5). https://doi.org/10.1029/2019JB018962

Dvory, N. Z., & Zoback, M. D. (2021). Prior oil and gas production can limit the occurrence of injection-induced seismicity: A case study in the Delaware basin of western Texas and southeastern New Mexico, USA. *Geology*, *49*, 1203. https://doi.org/10.1130/G49015.1

Ellsworth, W. L. (2013). Injection-induced earthquakes. *Science*, *341*(6142), 1225942. https://doi.org/10.1126/science.1225942

Enverus (1999). *DrillingInfo database*. Retrieved from https://www.enverus.com/

Eyre, T. S., Eaton, D. W., Garagash, D. I., Zecevic, M., Venieri, M., Weir, R., & Lawton, D. C. (2019). The role of aseismic slip in hydraulic fracturing-induced seismicity. *Science Advances*, *5*, eaav7172. https://doi.org/10.1126/sciadv.aav7172

Eyre, T. S., Zecevic, M., Salvage, R. O., & Eaton, D. W. (2020). A long-lived swarm of hydraulic fracturing-induced seismicity provides evidence for aseismic slip. *Bulletin of the Seismological Society of America*, *110*, 2205–2215. https://doi.org/10.1785/0120200107

Farahbod, A. M., Kao, H., Cassidy, J. F., & Walker, D. (2015). How did hydraulic-fracturing operations in the Horn river basin change seismicity patterns in northeastern British Columbia, Canada? *The Leading Edge*, *34*(6), 658–663. https://doi.org/10.1190/tle34060658.1

Frohlich, C., DeShon, H., Stump, B., Hayward, C., Hornbach, M., & Walter, J. I. (2016). A historical review of induced earthquakes in Texas. *Seismological Research Letters*, *87*(4), 1022–1038. https://doi.org/10.1785/0220160016

Frohlich, C., Ellsworth, W., Brown, W. A., Brunt, M., Luetgert, J., MacDonald, T., & Walter, S. (2014). The 17 May 2012 M 4.8 earthquake near Timpson, East Texas: An event possibly triggered by fluid injection. *Journal of Geophysical Research: Solid Earth*, *119*, 581–593. https://doi.org/10.1002/2013JB010755

Grandin, R., Vallée, M., & Lacassin, R. (2017). Rupture process of the mw 5.8 Pawnee, Oklahoma, earthquake from sentinel-1 InSAR and seismological data. *Seismological Research Letters*, *88*(4), 994–1004. https://doi.org/10.1785/0220160226

Guglielmi, Y., Cappa, F., Avouac, J.-P., Henry, P., & Elsworth, D. (2015). Seismicity triggered by fluid injection-induced aseismic slip. *Science*, *348*, 1224–1226. https://doi.org/10.1126/science.aab0476

Hanks, T. C., & Kanamori, H. (1979). A moment magnitude scale. *Journal of Geophysical Rsearch*, *84*(B5), 2348–2350. https://doi.org/10.1029/jb084ib05p02348

Hennings, P., Dvory, N., Horne, E., Li, P., Savvaidis, A., & Zoback, M. (2021). Stability of the fault systems that host-induced earthquakes in the Delaware basin of West Texas and southeast New Mexico. *The Seismic Record*, *1*(2), 96–106. https://doi.org/10.1785/0320210020

Hornbach, M. J., DeShon, H. R., Ellsworth, W. L., Stump, B. W., Hayward, C., & Frohlich, C., et al. (2015). Causal factors for seismicity near Azle, Texas. *Nature Communications*, *6*(6728), https://doi.org/10.1038/ncomms7728

Horne, E., (2020). "Data for: Horne et al. (2021) Basement-Rooted Faults of the Delaware Basin and Central Basin Platform, Permian Basin, West Texas and Southeastern New Mexico", Texas Data Repository, V2. https://doi.org/10.18738/T8/UHOUX8

Kanamori, H., & Anderson, D. L. (1975). Theoretical basis of some empirical relations in seismology. *Bulletin of the Seismological Society of America*, *65*(5), 1073–1095.

Keranen, K. M., Savage, H. M., Abers, G. A., & Cochran, E. S. (2013). Potentially induced earthquakes in Oklahoma, USA: Links between wastewater injection and the 2011 Mw 5.7 earthquake sequence. *Geology*, *41*(6), 699–702. https://doi.org/10.1130/G34045.1

Kim, J.-W., & Lu, Z. (2018). Association between localized geohazards in West Texas and human activities, recognized by Sentinel-1A/B satellite radar imagery. *Scientific Reports*, *8*(4727). https://doi.org/10.1038/s41598-018-23143-6

Kim, J.-W., Lu, Z., & Kaufmann, J. (2019). Evolution of sinkholes over Wink, Texas, observed by high-resolution optical and SAR imagery. *Remote Sensing of Environment*, *222*, 119–132. https://doi.org/10.1016/j.rse.2018.12.028

Kovach, R. L. (1974). Source mechanisms for Wilmington oil field, California, subsidence earthquakes. *Bulletin of the Seismological Society of America*, *64*(3), 699–711. https://doi.org/10.1785/bssa0643-10699

Lomax, A., & Savvaidis, A. (2019). Improving absolute earthquake location in West Texas using Probabilistic, Proxy ground-truth station corrections. *Journal of Geophysical Research: Solid Earth*, *124*(11), 11447–11465. https://doi.org/10.1029/2019jb017727

Lund Snee, J.-E., & Zoback, M. D. (2018). State of stress in the Permian Basin, Texas and New Mexico: Implications for induced seismicity. *The Leading Edge*, 127–134. https://doi.org/10.1190/tle37020127.1

Massonnet, D., & Feigl, K. L. (1995). Satellite radar interferometric map of the coseismic deformation field of the M = 6.1 Eureka Valley, California Earthquake of May 17, 1993. *Geophysical Research Letters*, *22*(12), 1541–1544. https://doi.org/10.1029/95gl01088

Okada, Y. (1985). Surface deformation due to shear and tensile faults in a half-space. *Bulletin of the Seismological Society of America*, *75*(4), 1135–1154. https://doi.org/10.1785/BSSA0750041135

Pepin, K. S., Ellsworth, W. L., Sheng, Y., Zebker, H. (2021). InSAR displacements in the Delaware basin TX (Version 2) [Data set]. Zenodo. https://doi.org/10.5281/zenodo.5842110

Pepin, K. S., Zebker, H. A., & Ellsworth, W. (2020). High-pass filters to reduce the effects of broad atmospheric contributions in SBAS inversions: A case study in the Delaware basin. In *IEEE international geoscience and remote sensing symposium*. https://doi.org/10.1109/IGARSS39084.2020.9324656

Savvaidis, A., Lomax, A., & Breton, C. (2020). Induced seismicity in the Delaware basin, West Texas, is caused by hydraulic fracturing and wastewater disposal. *Bulletin of the Seismological Society of America*, *110*(5), 2225–2241. https://doi.org/10.1785/0120200087

Savvaidis, A., Young, B., Huang, G.-c., & Lomax, A. (2019). TexNet: A statewide seismological network in Texas. *Seismological Research Letters*, *90*(4), 1702–1715. https://doi.org/10.1785/0220180350

Schultz, R., Skoumal, R. J., Brudzinski, M. R., Eaton, D., Baptie, B., & Ellsworth, W. (2020). Hydraulic fracturing-induced seismicity. *Reviews of Geophysics*, *58*. https://doi.org/10.1029/2019RG000695

Sheng, Y., Pepin, K. S., & Ellsworth, W. (2022a). On the depth of earthquakes in the Delaware basin—A case study along the Reeves-Pecos county line. *The Seismic Record*. https://doi.org/10.1785/0320210048

Sheng, Y., Pepin, K. S., & Ellsworth, W. (2022b). Relocated earthquakes along the Reeves-Pecos county line in the Delaware basin [Data set]. Zenodo. https://doi.org/10.5281/zenodo.5841588

Skoumal, R. J., Barbour, A. J., Brudzinski, M. R., Langenkamp, T., & Kaven, J. O. (2020). Induced seismicity in the Delaware basin, Texas. *Journal of Geophysical Research: Solid Earth*, *125*(1). https://doi.org/10.1029/2019JB018558

Staniewicz, S., Chen, J., Lee, H., Olson, J., Savvaidis, A., Hennings, P., & Jan, 27 (2021). Cumulative and transient surface deformation signals in the Permian Basin. *Earth and Space Science Open Archive ESSOAr*, https://doi.org/10.1002/essoar.10505979.1

Staniewicz, S., Chen, J., Lee, H., Olson, J., Savvaidis, A., Reedy, R., et al. (2020). InSAR reveals complex surface deformation patterns over an 80,000 km^2 oil-producing region in the Permian Basin. *Geophysical Research Letters*, *47*(21). https://doi.org/10.1029/2020gl090151

Starr, A. T. (1928). Slip in a crystal and rupture in a solid due to shear. *Mathematical Proceedings of the Cambridge Philosophical Society*, *24*(4), 489–500. https://doi.org/10.1017/S0305004100014626

Suckale, J. (2010). Moderate-to-large seismicity induced by hydrocarbon production. *The Leading Edge*, *29*(3). https://doi.org/10.1190/1.3353728

Teng, G., & Baker, J. W. (2020). Short-term Probabilistic hazard assessment in regions of induced seismicity. *Bulletin of the Seismological Society of America*, *110*, 2441–2453. https://doi.org/10.1785/0120200081

Texas Water Development Board. (2013). *Groundwater database (GWDB) reports*. Retrieved from http://www.twdb.texas.gov/groundwater/data/gwdbrpt.asp

U.S. Geological Survey, Earthquake Hazards Program. (2017). Advanced National Seismic System (ANSS). *Comprehensive Catalog of Earthquake Events and Products: Various*. https://doi.org/10.5066/F7MS3QZH

Weston, J., Ferreira, A. M., & Funning, G. J. (2012). Systematic comparisons of earthquake source models determined using InSAR and seismic data. *Tectonophysics*, *532–535*, 81. https://doi.org/10.1016/j.tecto.2012.02.001

Yeck, W. L., Hayes, G. P., McNamara, D. E., Rubinstein, J. L., Barnhart, W. D., Earle, P. S., & Benz, H. M. (2017). Oklahoma experiences largest earthquake during ongoing regional wastewater injection hazard mitigation efforts. *Geophysical Research Letters*, *44*(2), 711–717. https://doi.org/10.1002/2016GL071685

Zebker, H. A. (2017). User-friendly InSAR data Products: Fast and simple timeseries processing. *IEEE Geoscience and Remote Sensing Letters*, *14*(11), 2122–2126. https://doi.org/10.1109/LGRS.2017.2753580

Zhai, G., Shirzaei, M., & Manga, M. (2021). Widespread deep seismicity in the Delaware Basin, Texas, is mainly driven by shallow wastewater injection. *Proceedings of the National Academy of Sciences*, *118*(20). https://doi.org/10.1073/pnas.2102338118

Zheng, Y., & Zebker, H. A. (2017). Phase correction of single-look complex radar images for user-friendly efficient interferogram formation. *IEEE Journal of Selected Topics in Applied Earth Observations and Remote Sensing*, *10*(6), 2694–2701. https://doi.org/10.1109/JSTARS.2017.2697861

Zhu, W., Allison, K. L., Dunham, E. M., & Yang, Y. (2020). Fault valving and pore pressure evolution in simulations of earthquake sequences and aseismic slip. *Nature Communications*, *11*(4833). https://doi.org/10.1038/s41467-020-18598-z